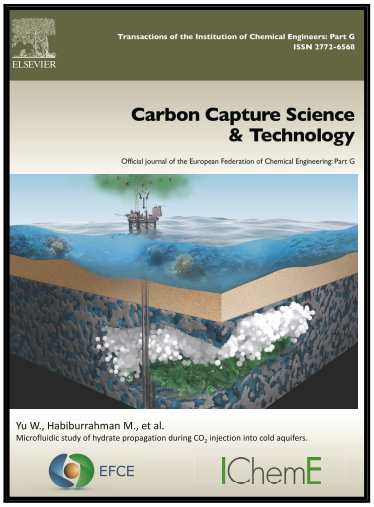

Olivine dissolution rates in wet CO_2 match or exceed aqueous rates

Mohamed A. Saleh , J.P. Martin Trusler , Mary P. Ryan , Nihal Darraj , Samuel Krevor

PII: S2772-6568(26)00115-6
DOI: https://doi.org/10.1016/j.ccst.2026.100682
Reference: CCST 100682

To appear in: *Carbon Capture Science & Technology*

Received date: 23 June 2026
Revised date: 25 August 2026
Accepted date: 27 August 2026

Please cite this article as: Mohamed A. Saleh , J.P. Martin Trusler , Mary P. Ryan , Nihal Darraj , Samuel Krevor , Olivine dissolution rates in wet CO_2 match or exceed aqueous rates, *Carbon Capture Science & Technology* (2026), doi: https://doi.org/10.1016/j.ccst.2026.100682

Highlights:

- First quantification of olivine dissolution rates in wet CO_2
- Olivine dissolution rates in wet CO_2 are up to 3.76x higher than aqueous rates
- Water-film mobility governs reactivity in wet CO_2 systems
- Direct CO_2 injection could substantially reduce water consumption

Olivine dissolution rates in wet CO_2 match or exceed aqueous rates

Mohamed A. Saleh [a*], J.P. Martin Trusler [b], Mary P. Ryan [c], Nihal Darraj [a] and Samuel Krevor [a]

[a] *Department of Earth Science & Engineering, Imperial College London, Exhibition Road, London SW7 2AZ, United Kingdom.*

[b] *Department of Chemical Engineering, Imperial College London, Exhibition Road, London SW7 2AZ, United Kingdom.*

[c] *Department of Materials Science, Imperial College London, Exhibition Road, London SW7 2AZ, United Kingdom.*

mohamed.saleh18@imperial.ac.uk, m.trusler@imperial.ac.uk , m.p.ryan@imperial.ac.uk, nihal.darraj20@imperial.ac.uk, s.krevor@imperial.ac.uk

Corresponding author: M. A. Saleh **Telephone:** +44 74 230 565 37

Postal address: Imperial College London, Exhibition Road, London SW7 2AZ, UK.

Abstract

Carbon dioxide injection into subsurface basalt, where it mineralises into carbonates, enables permanent emissions removal. Its scalability is limited by slow aqueous dissolution rates of metal silicate minerals, primarily olivine. Aqueous dissolution rate laws are well-established and apply to projects where CO_2 is dissolved in water before injection underground. An alternative approach reduces water consumption by directly injecting CO_2. However, mineralisation kinetics with CO_2-rich fluids are uncertain. Past observations are mostly qualitative and inconsistently report higher and lower reactivity compared to aqueous conditions. Here we quantify olivine dissolution rates using a novel plug-flow reactor setup in which capillarity is used to saturate a forsteritic olivine grain pack with CO_2, complemented by X-ray imaging. Co-injection of water and liquid CO_2 at elevated capillary pressure resulted in dissolution rates matching or exceeding aqueous rates, with rate enhancement of up to a factor of 1.1-3.76 depending on how the normalisation to surface area is treated. Conversely, limiting water mobility inhibited rates and is likely an explanation for past observations. Reactivity with liquid CO_2 is governed by the mobility of interfacial water films rather than total water content. Carbon mineralisation with the direct injection of CO_2 will have comparable or faster mineralisation as aqueous injection while requiring far less water.

Keywords

CO_2 Mineralisation, Dissolution rates, Reactive transport, Porous media, Olivine

1. Introduction

Carbon dioxide mineralisation in basaltic rocks offers a thermodynamically secure pathway for large-scale carbon sequestration, supporting the negative emissions targets of the Paris Agreement (Snæbjörnsdóttir et al., 2020). This process induces the dissolution of mafic silicate minerals in basalts, such as olivine, followed by reaction of the dissolved magnesium or calcium ions with the injected CO_2 to form solid carbonate minerals. As mineralisation progresses, carbon is permanently immobilised, eliminating the need for extended geophysical monitoring compared with other approaches to geological carbon storage, however, the risk of CO_2 leakage during the early stages of injection necessitates the presence of an effective caprock seal (Menefee et al., 2024).

While carbonation is thermodynamically favoured, the success of the technology depends on the rates at which reactions take place, and is limited by the initial dissolution of minerals (Gerdemann et al., 2007). In basaltic rocks targeted for mineral carbon sequestration, magnesium rich forsteritic olivine is the most reactive mineral phase and represents a key source of the metal cations needed for carbonation (Ratouis et al., 2022; Saleh et al., 2025). Studies using carbonated water (bulk aqueous solutions) have been used to characterise quantitative rate laws for the aqueous dissolution kinetics of olivine, the rate-limiting step in the overall carbonate formation (Gadikota et al., 2014; Johnson et al., 2014; Martinez et al., 2014; Matter et al., 2016; Luhmann et al., 2017; Wolff-Boenisch et al., 2018; Menefee et al., 2018; Wang et al., 2019; Wang et al., 2019b; Moita et al., 2020; Li et al., 2024). This aqueous environment is relevant to the operational approach that has underpinned the largest pilots of subsurface mineralisation, the Carbfix project in Iceland and 44.01 in Oman, where carbonated water is injected into the subsurface (Matter et al., 2016; Mahzari et al., 2025). The direct injection of CO_2 into the subsurface is also of interest because it can reduce both water consumption and total fluid injection rates by as much as 20 times relative to the injection of carbonated water, for the same amount of CO_2 sequestered (Snæbjörnsdóttir et al., 2020). Mineralisation reactions have been observed to take place in these environments where liquid or supercritical CO_2 interacts directly with the rock-forming minerals (Felmy et al., 2012; Loring et al., 2012; Schaef et al., 2013; Hua et al., 2015; Loring et al., 2019). Direct CO_2 injection has been piloted at the Wallula test site in the USA , with a series of basaltic caprock layers providing containment of the CO_2 plume during fluid-rock reactions (fig. 1) (Menefee et al., 2018).

However, the reaction kinetics in environments where the rock is in contact with liquid or supercritical CO_2 are uncertain (Abdolhosseini et al., 2022; Norton et al., 2024). Laboratory studies emulating this condition show that sub-micron scale water films act as the solvent medium through which reactants and products are transported to and from mineral surfaces (Felmy et al., 2012; Loring et al., 2012) (fig. 1). Quantifying the rates of reaction has been limited by the challenge of time-resolved sampling of these interfacial water films (Saleh et al., 2025). Studies have come to contradictory conclusions about whether rates are enhanced or inhibited in CO_2 rich environments relative to bulk aqueous kinetics (Felmy et al., 2012; Loring et al., 2012; Schaef et al., 2013; Loring et al., 2019; Saleh et al., 2024; Rajan et al., 2025; Rangel-Jurado et al., 2025). Many studies are performed in stirred batch reactors with poorly controlled water transport. Variability in reaction product transport away from reaction sites can have a large impact on observed dissolution rates and this is likely one source of the variable results reported in the literature. Thus, despite the implications for project design, it remains uncertain if the reactivity of a subsurface mineralisation site may be enhanced, inhibited, or remain unchanged if CO_2 is injected directly without first dissolving it into water.

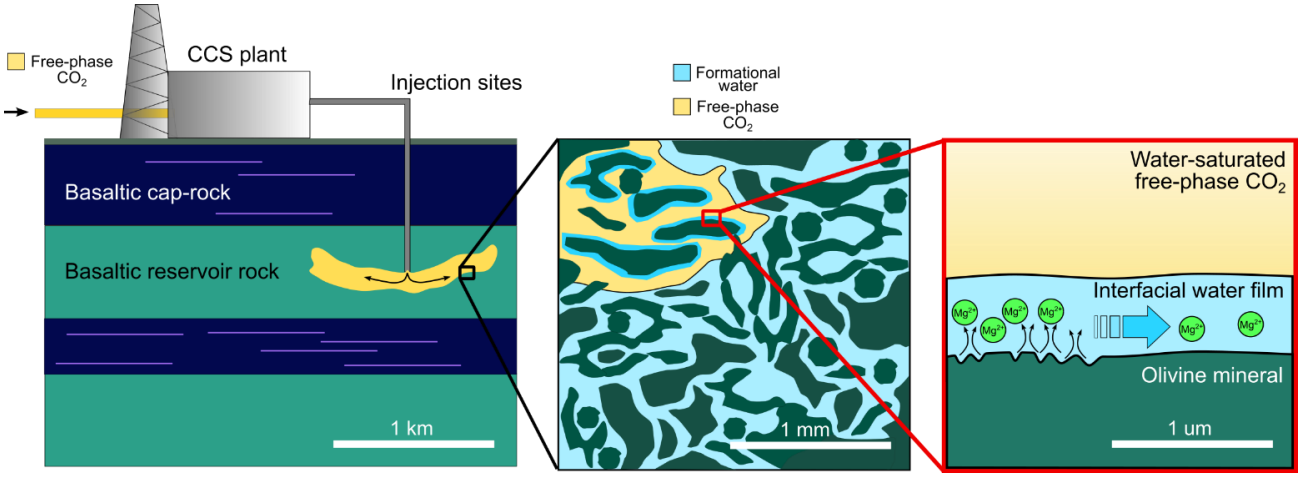

Figure 1. Schematic outlining the distinct reaction environments present in subsurface CO_2 injection sites and investigated in this study. The central panel reflects the condition of our experiment, where most pores are filled with water, and a minority filled with CO_2; the right-hand panel provides a close-up illustrating dissolution reactions taking place through the thin water films formed at the mineral surface in the presence of wet CO_2.

In this study, we developed a novel laboratory method with the aim of quantifying forsteritic olivine dissolution rates in the presence of water-saturated liquid CO_2. To achieve this, the multi-phase flow experimental method exploits capillarity to establish elevated CO_2 saturations representative of CO_2-rich flow conditions with reactions taking place in mobile interfacial water films at the mineral surface. *Operando* X-ray imaging was employed to determine the distribution of the fluid phases within the grain pack, enabling the mineral surface area in contact with the CO_2 phase to be quantified for rate normalisation. A separate set of experiments was then designed, with the secondary objective of isolating the influence of interfacial water film mobility on dissolution kinetics by comparing continuously replenished and stagnant water film conditions produced at mineral surfaces within the wet CO_2 environment. Rates derived from these experiments were compared against dissolution rates derived from a set of fully aqueous (carbonated water) benchmark control experiments. Reactive transport modelling provided the framework for establishing the aqueous benchmark and interpreting differences in reactivity. Our results show reaction rates with liquid CO_2 are at least equivalent to the bulk aqueous counterpart when thin water films are flowing, and possibly much higher. We also show that reaction rates when films are not flowing, and where reaction product transport is limited, are much lower than bulk aqueous rates, and this may be an explanation for past observations. Together, these observations provide new insight into the fundamental chemical processes governing mineral dissolution in CO_2-rich environments and demonstrate that direct injection of free-phase CO_2 can sustain reaction rates comparable to those observed under fully aqueous conditions. This creates the opportunity for reductions in water consumption and total fluid injection rates into the subsurface during carbon mineralisation.

2. Experiments

2.1 Materials

Magnesium-rich (forsterite) olivine grains originating from Åheim Forsteritic Dunite rock (unserpentinised) was supplied by Sibelco Nordic AS, Norway. X-ray diffraction (XRD) was

employed to analyse the mineralogy of olivine used in our experiments (supplementary figure A1). In addition to Forsterite, accessory minerals clinochlore and enstatite were detected and matched to our XRD pattern using the ICDD library. Forsteritic olivine is both the dominant phase and the most rapidly dissolving constituent under the experimental conditions and is therefore expected to account for the large majority of the measured Mg^{2+} release; contributions from the less abundant clinochlore and enstatite phases are considered minor (Palandri and Kharaka, 2004). Rietveld refinement was conducted on the matched mineral phases to calculate mineral fractions by weight and indicated bulk forsterite olivine composition (Table 1). A refined forsteritic olivine composition of Fo93 was also calculated ($Mg_{1.85}Fe_{0.15}SiO_4$). This value is similar to the average olivine composition calculated in previous studies utilising Åheim forsterite (Keefner et al., 2011; van Noort et al., 2013).

Table 1 – Olivine grain composition

Mineral phase	Abundance (wt.%)
Forsterite olivine	77
Clinochlore	14
Enstatite	9

The olivine grains were sieved through a 300um sieve 20 times using a Retsch sieve shaker until no powder filtered through. The fraction of olivine grains coarser than 300um was retained for use in experiments. This fraction was ultrasonicated in absolute ethanol 25 times to remove adhered fines until the supernatant remained clear. The olivine was dried overnight in a vacuum oven at 60 °C. Particle size distribution was analysed using a Malvern Mastersizer 3000E instrument (fig. 2). BET specific surface area (SSA) analysis was conducted on this olivine size-fraction using an Autosorb iQ Quantachrome instrument. BET SSA was calculated to be 0.058 m^2g^{-1} (Table 2).

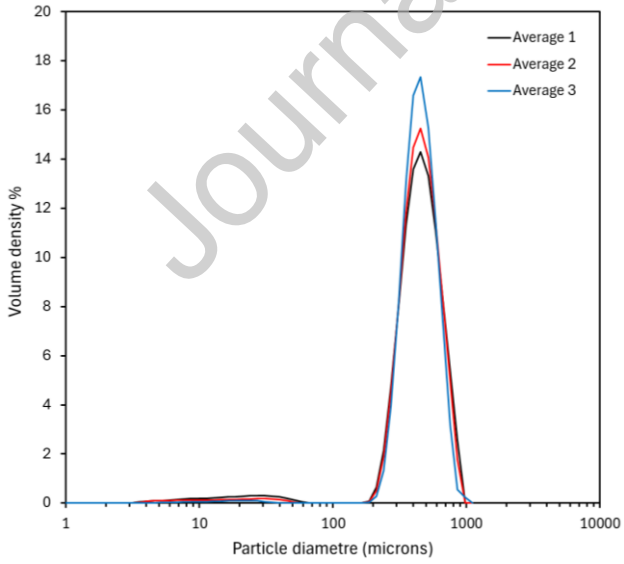

Figure 2. Olivine grain size characterisation. Three averages are shown, each from 10 repeat measurements of cleaned olivine particle size distributions shown as a volume density versus particle size plot.

Table 2 – Olivine properties

Material property	Measurement

BET SSA (m^2g^{-1})	0.058
Specific gravity (gcm^{-3})	3.25
d10 (µm)	310
d50 (µm)	474
d90 (µm)	711
Sample mass (g)	1.429 ±0.007

2.2 Flow reactor system

Carbon dioxide (99.995% purity) and de-ionised water (18.2 MΩ cm) are the only fluids used in this study. A liquid state CO_2-rich phase was chosen over supercritical CO_2 due to its greater stability at room temperature under lower pressure conditions. This stability facilitates controlled experimental conditions and enhances reproducibility in sequestration studies. Liquid CO_2 also maintains a water-saturation capacity (2.72-3.07 mol H_2O per 1000 mol CO_2) in the same order of magnitude as that of supercritical CO_2 (3.84 mol H_2O per 1000 mol CO_2) (King et al., 1992).

To sustain CO_2 in a liquid state, a Huber microprocessor chiller unit was connected to two CO_2 ISCO 1000D pump jackets (fig. 3). A 50% mixture of ethylene glycol and de-ionised water was circulated through the pump jackets at a set temperature of 5°C. This temperature enables CO_2 to be supplied in a liquid state from the source to the pumps at 50 bar and prevents phase transitions occurring inside the pumps during pressurisation. Pressure is then increased to 70 bar, ensuring experimental conditions reside within the liquid CO_2 phase envelope at room temperatures of 22-25ºC. The CO_2 phase was maintained in constant contact with DI water within a Parr Model 4540 reactor at experimental conditions (Table 3) to ensure carbon dioxide-rich liquid in equilibrium with water-rich liquid is available throughout injection (Aavatsmark et al., 2015). A 4540 model Parr reactor is half-filled with DI water prior to equilibration with CO_2. Liquid CO_2 volume is allowed to stabilise inside the pumps before introducing flow into the reactor headspace where the two fluids contact one another prior to injection. Equilibration time is set to 10 days with constant stirring to allow sufficient time for mutual solubility limits to be reached and PID control oscillations to have fully stabilised (supplementary figure A2). To prevent overnight temperature fluctuations, reactor temperature was maintained at the upper-end of room temperatures (25℃). During experiments where both water and CO_2 injection is necessary, a separate H_2O-filled ISCO 1000D pump is used to drive injection, and the CO_2-filled ISCO pumps are used to drive liquid CO_2 injection (fig. 3).

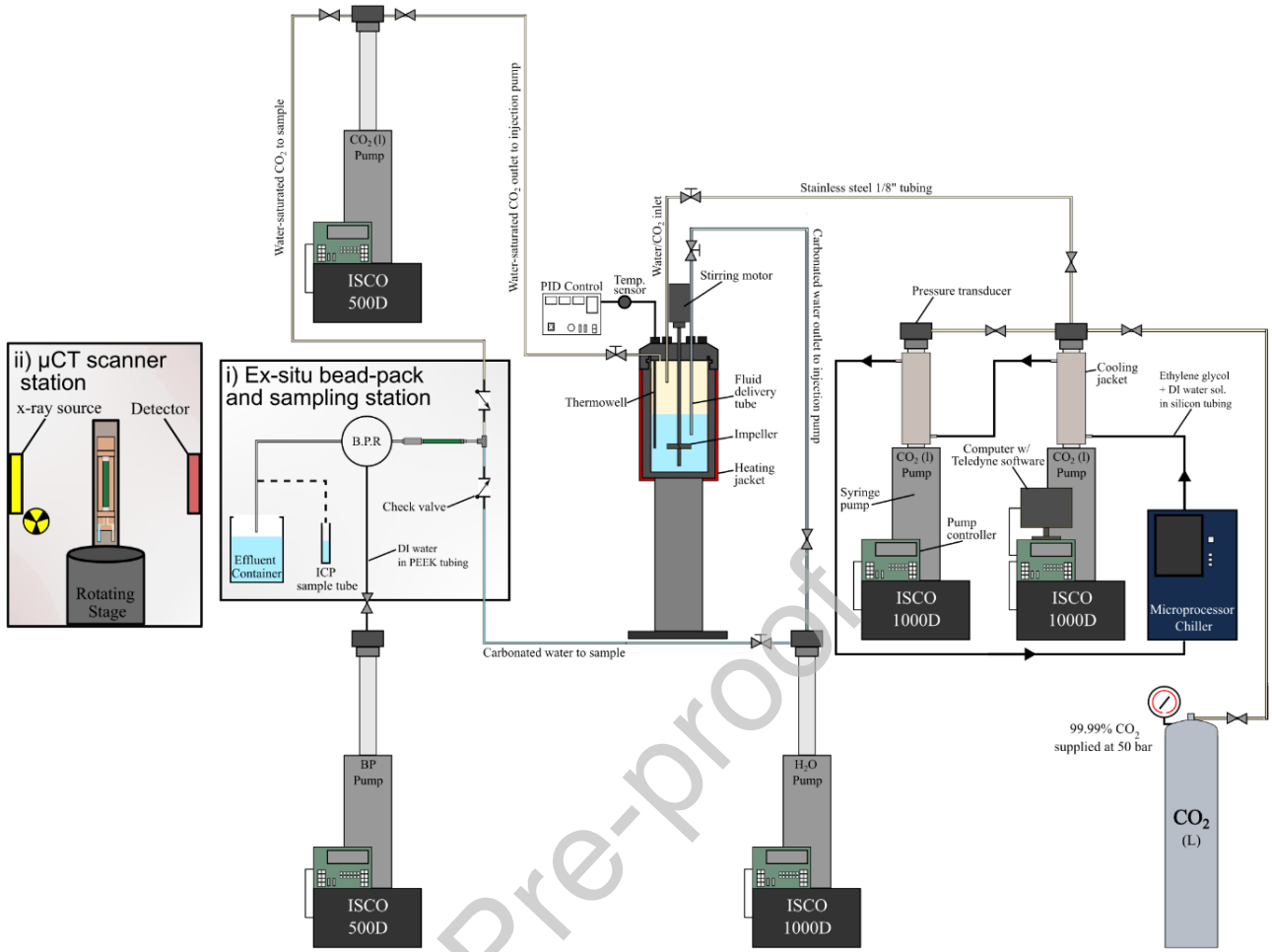

Figure 3. Experiment process flow schematic for single-phase and co-injection high-pressure flow-through experiments operated on a bench setup (i), and then adapted to fit into a micro-focus X-ray CT operando imaging setup (ii).

In total, three distinct CO_2-water fluid injection experiment branches are investigated (Table 3). Experiments in each fluid regime are repeated to produce a total of six bench experiments measuring magnesium ion (Mg^{2+}) release rates. The same set of reaction conditions were applied across all runs (Table 3). The fluids injected through the sample pack is the sole variable in our experiments.

Table 3 – Experimental conditions

Primary fluid injected	Temperature (°C)		Pressure (bar)	Flowrate water (mL min^{-1})	Flowrate CO_2 (mL min^{-1})	Eqm. time (days)	Injection Duration (days)
	Reactor interior	Sample vessel exterior					
Control 1: Carbonated water (CW1,2)	25	18.4 (±0.9)	70 (±1)	0.2	-	10	5
Control 2: Co-injection without porous plate (FF1)	25	18.4 (±0.9)	70(±1)	0.2	0.6	10	3
Co-injection with 0.5bar Pc porous plate (FF3,4)	25	18.4 (±0.9)	70(±1)	0.2	0.05	10	3
Co-injection with 1bar Pc porous plate (FF5,6)	25	18.4 (±0.9)	70(±1)	0.2	0.05	10	3
Co-injection with 1bar Pc porous plate and high	25	18.4 (±0.9)	70(±1)	0.2	1.0	10	3

CO_2 flow rate (FF7)							
Alternating injection (ALT1,2)	25	18.4 (±0.9)	70 (±1)	-	0.2	10	5

Note: Each experiment type was repeated to demonstrate repeatability of results. Pc refers to the capillary entry threshold of each porous plate.

The first pair of experiments involve bench tests assessing Mg^{2+} release under single-phase carbonated water flow at 0.2 ml/min. The second pair involve the injection of alternating single-phase liquid CO_2 (which had been equilibrated with water prior to injection) and carbonated water (both at 0.2 ml/min). In both these experiments, olivine samples were housed within a quarter-inch austenitic steel tubing adjacent to a Swagelok 15 µm inline filter designed to resemble a plug-flow reactor scheme. External sample vessel temperature was monitored using a ThermoWorks laser thermometer throughout all experiments. The filter chamber was filled with ThermoFischer glass wool filter aid to act as a physical buffer between the powder and the filter element, mitigating potential filter cake formation. A filter-aid was necessary after failed attempts stemming from over pressurisation due to filter blockages. Downstream of the filter, a custom-built back-pressure regulator is incorporated, enabling the continuous flow of high-pressure liquid CO_2 and carbonated water within our target range of flow rates, without incurring damage to water freezing during fluid depressurisation at the outlet. An ISCO 250D pump is setat constant pressure mode to apply a fixedpilot pressure on the back-pressure regulator diaphragm throughout each experiment. Where Hastelloy tubing could not be used, PEEK flow line connections are utilised instead throughout the setup.

A third pair of experiments involves co-injection of water-saturated liquid CO_2 and carbonated water. Co-injection experiments were conducted once without a porous plate as a control. In this setting, CO_2 saturations (S_{CO_2}) are very low, $S_{CO_2} < 0.1$, due to the weak capillarity of the grain pack and the low viscosity of CO_2 relative to water. Co-injection experiments were then carried out using a water-wet micro-porous ceramic plate to create a controlled increase in CO_2 saturation within the olivine grain pack (fig. 4). Elevated liquid CO_2 saturations arise from the higher capillary entry pressure of the porous ceramic plate relative to the packed olivine bed. This capillary-pressure contrast restricts the passage of the non-wetting CO_2 phase through the porous plate, causing CO_2 to accumulate upstream and establish elevated liquid CO_2 saturations within the olivine pack under steady-state flow conditions. The capillary entry thresholds (Pc) of the plates utilised vary from 0.5, and 1 bar (Table 3). Water flowrates of 0.2 ml/min were again applied to maintain a comparison with all other experiments, and a CO_2 flowrate of 0.05ml/min was applied to ensure a steady supply throughout. A further 1bar plate experiment was conducted using a flowrate of 1ml/min CO_2 to investigate high-flow (HF) conditions.

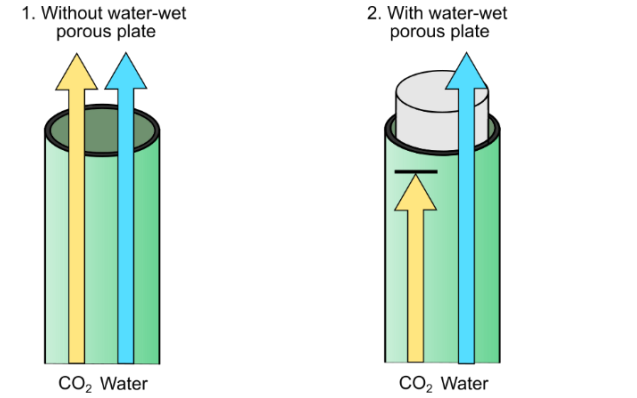

Figure 4. Schematic illustrating the effect of including the ceramic water-wet porous plate on fluid flow and CO_2 saturation within the olivine grain pack (17%) during two-phase flow co-injection experiments.

Experiments without the porous plate were conducted using the setup shown in figure 5a. Experiments including a porous plate required a modified setup involving an external core-holder. The core holder contains a nitrile sleeve that houses the olivine grain pack and porous plate and is sealed onto two PEEK pistons with fixed tubing at either end (fig. 5b). PEEK filters were designed and placed at either end of the grain pack to securely retain the olivine grains within the sleeve while maintaining unobstructed fluid flow. The PEEK reactor casing was also utilised for the micro-focus X-ray CT experiments to avoid interference from steel components during imaging (fig. 5b). Both reactor configurations were designed with an identical grain-pack pore volume of 0.4 mL. A differential pressure transducer is incorporated across the two inlet lines to monitor the liquid CO_2 inlet pressure buildup and subsequent break-through point across the plate, after which a stable pressure was maintained and sampling conducted. Sleeve length, diameter and sample mass was matched across both setups.

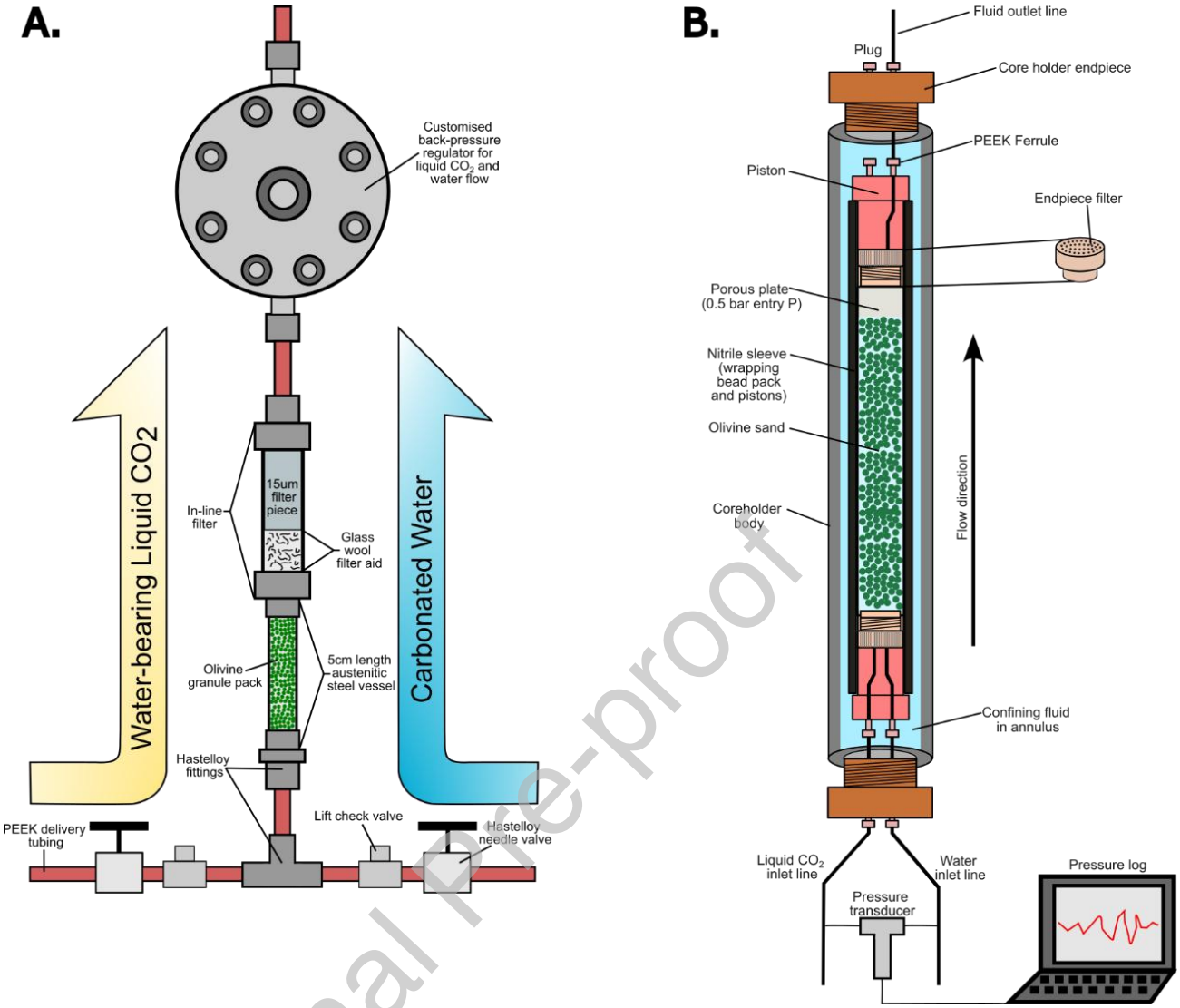

Figure 5. Schematics showing grain pack setups. A) Hastelloy and austenitic steel vessel (grain pack) and in-line filter setup equipped with a custom-built back-pressure regulator designed to enable constant single-phase flow, alternating fluid flow, and fractional flow high-pressure experiments involving carbonated water and liquid CO_2. B) Micro-Core-holder and custom PEEK grain pack design utilised for experiments carried out with porous plates and within the CT scanner.

2.3 Validation of experimental approach

Single-phase carbonated water experiments serve as control tests in this study (fig. 6). By plotting this data against the number of injected water pore volumes we demonstrate that we are comparing these experiments on an equivalent water-mass basis. We validate our approach by predicting the corresponding experimental concentration data using established olivine aqueous dissolution rate parameters of Hänchen et al. (2006) within a PHREEQC 1D reactive transport simulation code. The pH in both carbonated water experiments was simulated to range from 3.2-3.3. The model is discretised to match our setup geometry and fluid flow rates, ensuring a mechanistic representation of our flow-through system. As a result, our model does not employ any fitting parameters. However, the model does not match the sharp drop in Mg^{2+} concentration observed at the start of the reaction time (first 10 hours of reaction), likely caused by fine particle dissolution (Metz et al., 2001; Chen et al., 2025).

Fines typically adhere onto larger grain surfaces during sample cleaning procedure making complete eradication of fine particle populations difficult. The fines population is shown in figure 2.

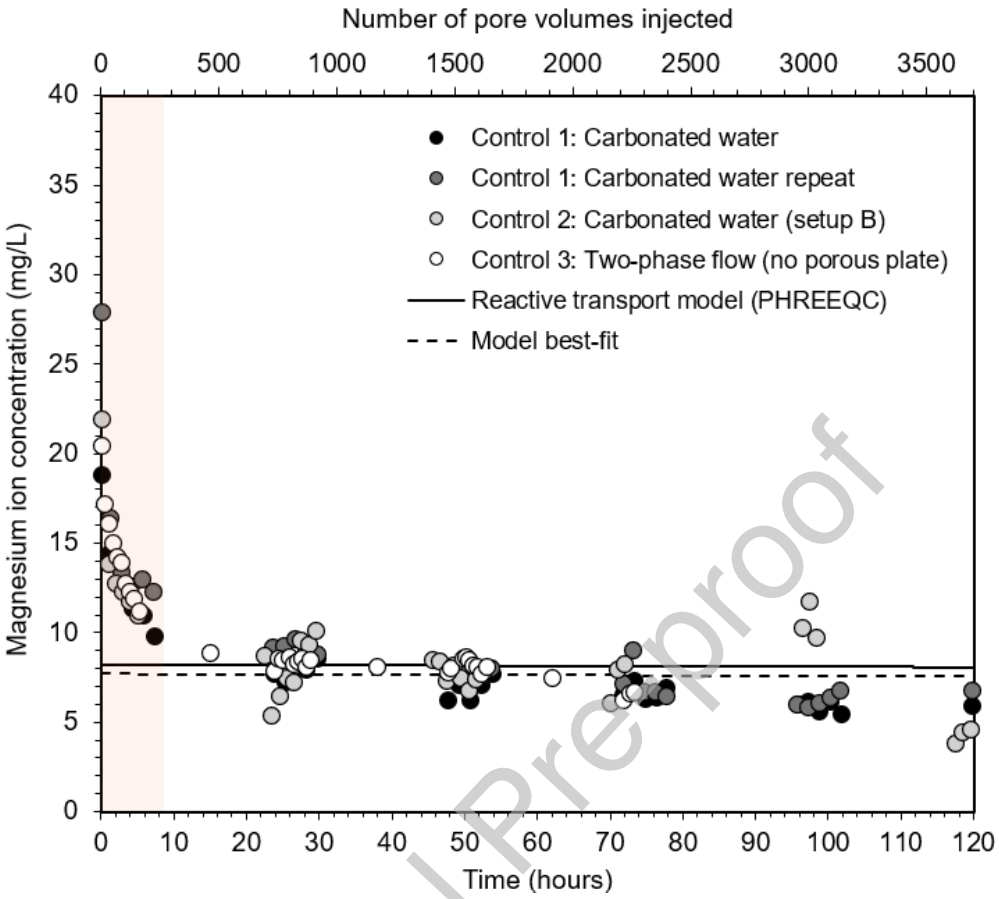

Figure 6. Magnesium concentrations obtained from control experiments, plotted against time and number of pore volumes injected with carbonated water. The PHREEQC reactive transport model is shown as a solid black line. The best-fit version of the PHREEQC model is shown by a dashed line for reference (normalised root mean square error of model = 0.18) and represents the deviation from our PHREEQC model to the version that minimises least squares error. The best fit is calculated using 0.925x the rate of the PHREEQC model. The first 10 hours of initially high Mg^{2+} signatures in all experiments are shaded. Note: Setup B is illustrated in figure 5.

The second control experiment utilised in our study was the two-phase (carbonated water and water-saturated liquid CO_2) co-injection flow experiment without the porous plate, such that the CO_2 saturation remained very low. The experiment used a 3:1 CO_2 to water volumetric flowrate ratio (experiment FF1) with the water rate maintained at 0.2 ml min^{-1} as with the other experiments. The results of this control are indistinguishable from the carbonated water controls (fig. 6). This control experiment was performed to validate the need for the porous plate to establish elevated liquid CO_2 saturations (fig. 4), ensuring that the measured dissolution kinetics, measured in the subsequent co-injection experiments, reflect the intended capillary-controlled flow conditions rather than viscosity-dominated flow. A further control experiment (FF2) was then conducted to validate the alternate reactor configuration (setup B) shown in fig. 5b, which was used for the operando imaging and porous plate experiments. This control experiment confirms that the same benchmark single-phase

carbonated water dissolution behaviour can be reproduced in setup B as that observed in the initial setup, before proceeding to the co-injection experiments.

2.4 Micro-focus X-ray CT imaging for co-injection experiments

Imaging of one of the co-injection experiments with a porous plate was performed using a Bruker SKYSCAN 1273 micro-focus X-ray CT following a protocol:

1. The setup shown in figure 5b was fitted onto the rotating scanner stage and PEEK tubing was connected at inlets and outlets to external pumps ensuring pressure and flowrate was controlled during fluid delivery. A porous plate positioned at the outlet end of the grain pack.
2. A confining pressure of 100 bar was applied, ensuring the sleeve tightly enveloped the olivine grains, thereby preventing fluid bypass. Nitrogen leak tests were conducted to ensure that the confining fluid does not have a pathway to go through the sample, hence it does not contaminate it.
3. The scanning parameters were adjusted, a filter of copper and aluminium (Cu+Al) with a 0.05 thickness was applied. The filter helps in reducing the noise and improving the image quality. The dry sample was then imaged using a full-length (35mm) spiral continuous scan with a resolution of 9.5 μm per voxel and 3600 projections. Note: This voxel size does not resolve the sub-micron features.
4. The sample was initially flushed with gaseous CO_2 to replace the air and ensure full saturation once the brine is introduced. The carbonated KI solution was then injected to saturate the sample at 0.2ml/min and 70 bar, until effluent passed through the back-pressure regulator, ensuring complete water saturation and no residual air pockets. A visual check on the images was carried out confirming no air pockets in the sample. A brine scan was then taken using the same scan mode.
5. Liquid CO_2 was injected at a maximum injection rate of 0.05 ml/min and matching pressure through an ISCO pump. The pressure difference across the rock sample was continuously monitored using a pressure transducer. This allowed for the observation of the CO_2 break-through and subsequent steady-state pressure across the sample. After allowing the system to flow for one hour, a final scan was performed to image the two-phase system.
6. Post scanning, the CO_2-brine-olivine image was masked with the image of the separated pores, the fluid distribution in each pore region is obtained. The fluid-fluid and fluid-solid interfaces are identified and extracted by a voxelized surface generation algorithm and smoothed with an iterative algorithm preventing boundary shrinking (Garfi et al., 2022).

2.5 Effluent collection and analysis

During each experiment, effluent samples were collected at regular intervals. Outlet tubing was sealed to the lids of collection vessels to nullify loss of fluid due to pressure release bursts during delivery. Samples were filtered through 0.2-micron filters and weighed prior to analysis. Standard concentration solutions were prepared from deionised (18 MΩ) using VWR ARISTAR quality control standard 100 mg/l in nitric acid 5%. The Mg^{2+} concentration

in effluent solutions was determined using a PerkinElmer Avio 500 Inductively Coupled Plasma Optical Emission Spectroscopy (ICP-OES) against the aqueous standards (supplementary figs. A3, A4, supplementary table A1). Relative Standard Deviations (RSDs) are calculated from 3 replicate measurements of each sample collected (supplementary table A2). Fe concentrations were not reported as they consistently fall below the reliable detection limit (~1ppm at most).

During alternating liquid CO_2 injection experiments, controlled water flushes were carried out at each sampling interval to flush out all solutes released from the dissolution of olivine in presence of CO_2 (fig. 7). Flowrates and pressures were maintained during these water flushes and water was collected at the outlet. Fractional flow experiments where both phases were co-injected through the grain-pack resulted in intermittent fluid bursts at the outlet, requiring a sealed lid to be fitted onto the sample collection vessel to avoid fluid loss.

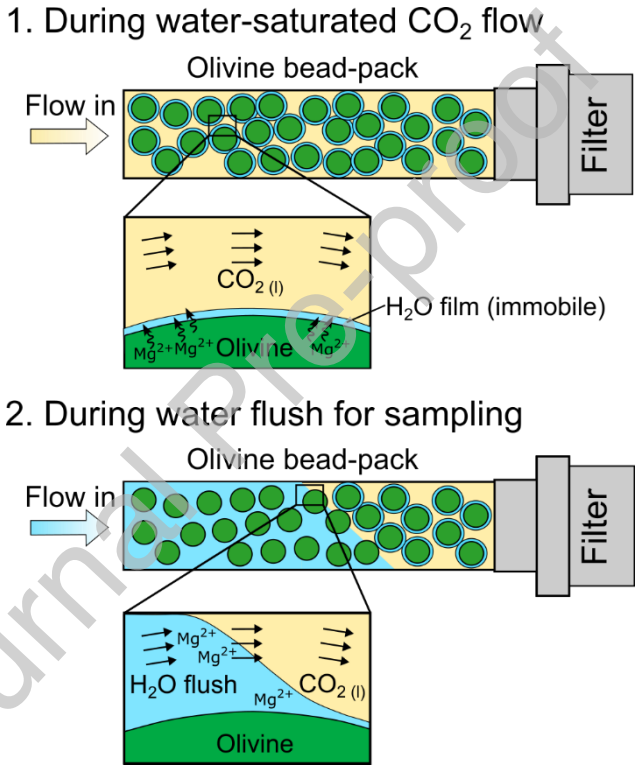

Figure 7. Schematics outlining a systematic water flushing procedure utilised for sample collection during liquid CO_2 experiments, assuming spherical grains for simplicity.

2.6 Reactive transport modelling framework

Mineral dissolution and solute transport were simulated using PHREEQC v3.8.2 (Parkhurst and Appelo, 2013). The geochemical model presented here was developed to reproduce the continuously flowing bulk aqueous dissolution experiments and provide a benchmark for comparison with the two-phase co-injection experiments. The column was represented as a sequence of fully mixed cells. Transport was solved using PHREEQC's cell-based advection scheme, and mineral dissolution was explicitly integrated within each cell at every advective timestep.

Influent water solution blocks were defined at 25 °C and equilibrated with CO_2 at $\log_{10}pCO_2$ = 1.84, matching experimental conditions without fitting any parameters or imposing specific pH conditions. The upstream boundary solution (feed solution 0 at x=0) was defined identically. All solutions were specified on a molality basis (mol kg^{-1} water).

The model column geometry matched the experimental flow-through reactor. A measured porosity of 47% yielded a pore volume per cell of ~0.45mL. A 5-day experiment (432,000 s) was simulated under the imposed 0.2 mL min^{-1} flow. Flux boundary conditions were applied at both inlet and outlet, consistent with a constant-flow open system. Longitudinal dispersivity was switched off as this is negligible at laboratory scale. Molecular diffusion was included (D = 0.78×10^{-9} m^2 s^{-1}) for Mg^{2+} ions in aqueous solution (Harned and Owen, 1958).

Forsterite dissolution was modelled kinetically using the rate law:

$R = rA_{tot}$ (eq. 1)

$r = k\, a_{H^+}^{n} \exp(-\frac{E}{RT})\,(1 - \mathrm{SR})$ (eq.2)

Where k , n and E follow forsterite rate parameters in the range quoted in Hänchen et al. (2006), SR is the saturation ratio of forsterite, A is the evolving reactive surface area. An assumption to relate the total surface area (A_{tot}) of dissolving particles to their volume and thereby mass is implemented using a scaling factor (p) of 0.79 which depends on the particle-size distribution (Hänchen et al., 2006):

$A = A_0(\frac{M}{M_0})^p$ (eq. 3)

with M the remaining mineral moles. BET-measured initial surface areas were included through the *KINETICS* block. Mineral dissolution was integrated over each advective timestep using a Runge-Kutta solver. All calculations used PHREEQC's internal temperature, pressure, and activity models, with kinetic tolerance set to default.

Effluent Mg concentrations were monitored from the outlet cell at each advective shift along with system pH evolution. Dissolution rates were extracted from PHREEQC based on the kinetic reactant mole balance normalised by the reactive surface area to obtain surface-normalised dissolution rates in mol m^{-2} s^{-1}.

Equations 4-7 used to calculate the ratio between reaction rates in two-phase co-injection experiments and carbonated water experiments. To quantify the relative reactivity in the two-phase co-injection experiments compared with the carbonated water experiments, we express the overall reaction rate, R, as the sum of contributions from mineral surface in contact with CO_2 and aqueous fluid:

$R = r_{CO2}(X_{CO2}A_{tot}) + r_{aq}(X_{aq}A_{tot})$ (eq. 4)

where r_{CO_2} and r_{aq} are the intrinsic reaction rates in the CO_2 and aqueous environments, respectively, A_{tot} is the total reactive surface area, and X_{CO_2} and X_{aq} are the fractions of surface area associated with each fluid phase (see Results section 3.1).

Expressing the measured bulk rate enhancement, z, relative to the aqueous reaction rate gives:

$z(r_{aq}) = r_{CO2}X_{CO2} + r_{aq}(1 - X_{CO2})$ (eq. 5)

Substituting the average enhancement factor from all three pairs of repeat co-injection experiments (see Results section 3.1) relative to the best-fit bulk aqueous dissolution model measured enhancement factor, z, yields:

$z = \frac{r_{CO2}}{r_{aq}}X_{CO2} + 1 - X_{CO2}$ (eq. 6)

which can be rearranged to solve for the ratio of intrinsic reaction rates in the two environments:

$\frac{r_{CO2}}{r_{aq}} = \frac{z-1}{X_{CO2}} + 1$ (eq. 7)

To quantify differences in rates between the baseline (fully aqueous) model and two-phase injection experiments, the base carbonated water injection model was multiplied by a scaling factor to fit each pair of repeat datasets. The agreement between PHREEQC model predictions and experimental Mg concentration data was evaluated by determining an optimal least-squares scaling factor, k, for each combined repeat dataset. Model outputs were interpolated onto the experimental time points, and k was calculated analytically by minimizing the sum of squared residuals between model and experiment. (eq. 8). This approach ensures that all replicate measurements contribute simultaneously to the fit, providing an unbiased assessment of model performance. Model accuracy was quantified using the sum of squared errors (SSE), root mean square error (RMSE), and normalized RMSE (NRMSE), with the latter expressing the average deviation relative to the mean experimental concentration and enabling comparison across conditions.

$k = \frac{\sum(C_{\text{exp}} \cdot C_{\text{model}})}{\sum(C_{\text{model}}^2)}$ (eq. 8)

2.7 Plug Flow mole balance for experiments with alternating flow

The mole balance expression describing a plug flow tubular reactor was utilised to compute dissolution rates obtained from our alternating injection (ALT1, ALT2) experiment system (eq.9).

$r_A = \frac{dF_A}{dV}$ (eq. 9)

Where F_A represents the molar flow rate calculated using experimental flowrates of carbonated water used in all experiments except alternating liquid CO_2 flow (where water flow was minimal by comparison to CO_2). V represents the total tubular reactor internal volume as per our design specifications. This rate was then adjusted to account for the volume occupied by mineral grains. However, the volume occupied by olivine grains, and the surface area of these grains is not fixed and changes with each leaching time step. To account for the changing surface area of grains throughout the experiment; we first calculate the mass

of grains remaining after known experimental concentrations of magnesium are leached at each time step by fitting a linear piece-wise regression for each dataset containing aqueous flow components (supplementary figure A5).

Numerical integration of these models, considering the experimental flowrate (Q), provides the mass of magnesium leached ($M_{Mg(t)}$) at each time step. The remaining total mass of magnesium can then be calculated by deduction. This enables us to quantify the impact of particle-size reduction on 1) the corresponding mass of olivine mineral remaining at each time step (M_{rem}) (eq. 10), and 2) the surface area, in turn providing the effective surface area required for deriving the dissolution rate at each time step (eq. 11).

$$M_{rem} = M_0 - \frac{M_{Mg(t)}}{xMg_{ol}} \text{ (eq. 10)}$$

Where xMg_{ol} is the mass fraction of magnesium in our olivine grains.

$$SA(t) = SSA \cdot M_{rem} \cdot \left(\frac{M_{Mg(t)}}{M_{Mg,0}}\right)^{p} \text{ (eq. 11)}$$

M_0 is the initial sample mass, SSA is the initial BET specific surface area (m^2g^{-1}), and the term $(M_{Mg(t)}/M_{Mg,0})^p$ represents a geometrical scaling factor accounting for the change in particle size as magnesium is removed from the mineral (Hänchen et al., 2006). The following assumptions are made to validate the use of equation 11: 1) Magnesium loss proportionally reflects solid phase retreat. That is, the extent of Mg removal is considered representative of the retreat or dissolution of the particle surface. 2) The magnesium is assumed to be evenly dispersed within the mineral particles such that it's leaching leads to uniform reduction of the solid phase, rather than localized depletion or selective surface modification. 3) Magnesium leaching is the dominant mechanism of structural change 4) No significant new surface formation occurs.

3. Results

3.1 Quantifying reaction rates in wet CO_2 environments

Experiments were carried out by simultaneous injection of water and CO_2, pre-equilibrated with each other, at 25 ℃ and 70bar (7MPa), through a cylindrical column of crushed olivine grains. These two-phase co-injection (carbonated water and wet liquid CO_2) experiments were conducted using porous plates rated to 0.5bar (labelled FF3 and FF4) and 1bar (labelled FF5 and FF6) capillary pressures to create higher CO_2 saturation of the pore space between olivine grains as compared with control experiments (labelled CW1, CW2), and one additional experiment was conducted with a higher CO_2 volumetric flowrate (labelled FF7).

The 0.5bar capillary pressure experiment was imaged *in situ* using micro- focus X-ray CT. Under the elevated capillary pressure condition, CO_2 is distributed throughout the length of the olivine grain pack (fig. 8). The average CO_2 saturation (the fraction of the pore space filled with CO_2 versus water) across the sample was $S_{CO_2} = 17\%$.

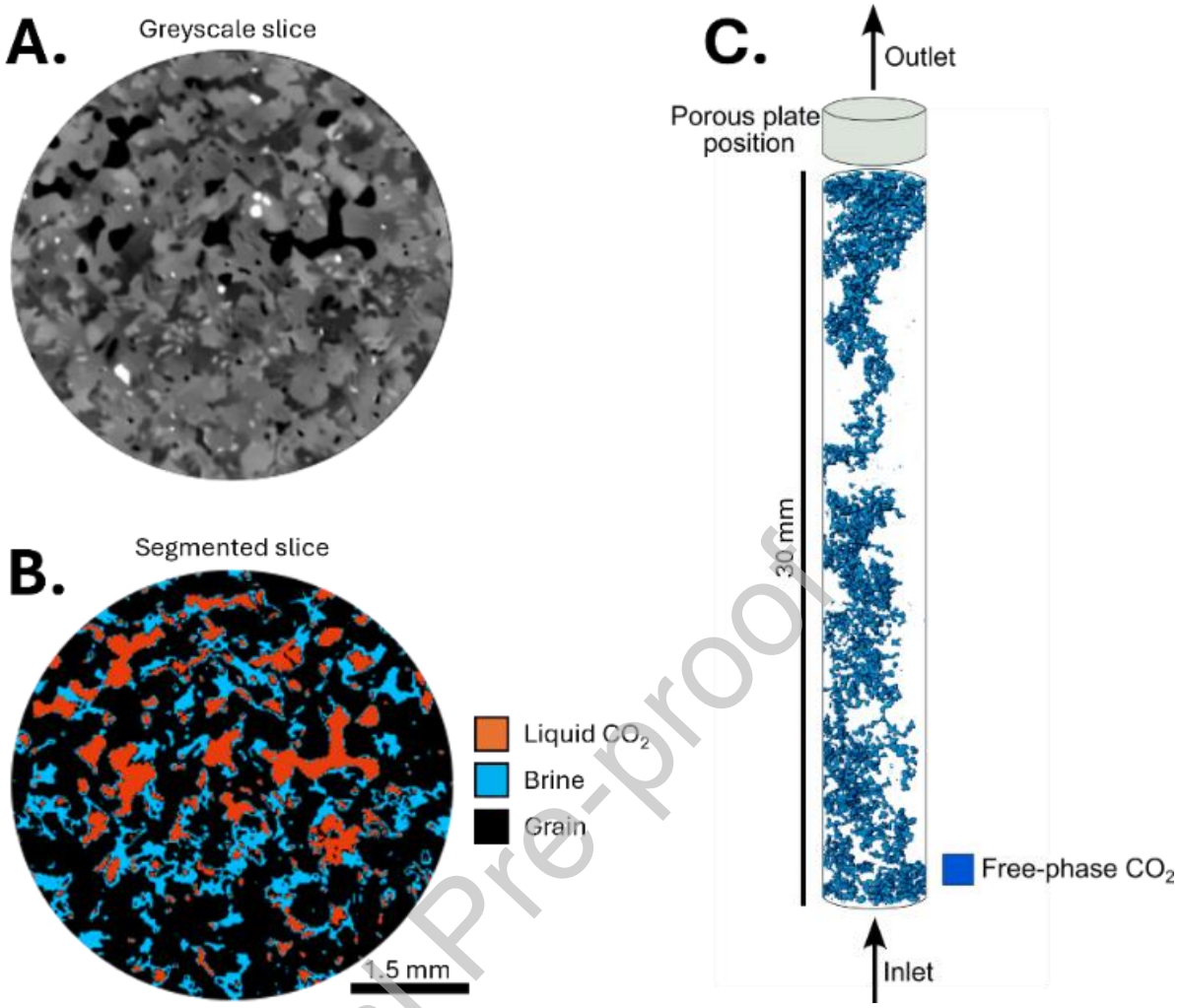

Figure 8. A.) 2D cross sections of 3D raw and segmented images of the olivine grain pack at a 9.5 µm/voxel resolution. B.) Grey-scale cross-section image of the olivine grain pack after non-local means filter for removing noise was applied shows the liquid CO_2 (dark), the carbonated KI solution (grey) and the grain (bright). The segmentation process consists of assigning each voxel (3D pixel) of the image to an individual phase identified by a numerical index. The segmented image shows liquid CO_2, KI solution, and olivine grains. C) 3D visualisation confirming the percolation of liquid CO_2 throughout the entire volume of the olivine grain pack during steady-state two-phase flow post pressure break-through, showing the impact of the porous plate in elevating CO_2 capillary pressure on the physical distribution.

While the specific surface area of the minerals was measured using standard techniques (see section 2.4), the relative fraction of interfacial surface area between water-grain and CO_2-grain contacts was measured from the imaging data and are shown in figure 9. The percentage of olivine grain surface area contacting water-saturated liquid CO_2 during steady-state flow (example shown in fig. 9d), is calculated at 5.2% (±0.26) of the total surface area, accounting for 5% uncertainty in segmentation (35,597 ±1780 voxels out of a total 684,253). This relationship whereby the surface area coverage is significantly lower than the fluid saturation is characteristic of water-wetting porous media (Garfi et al., 2020b).

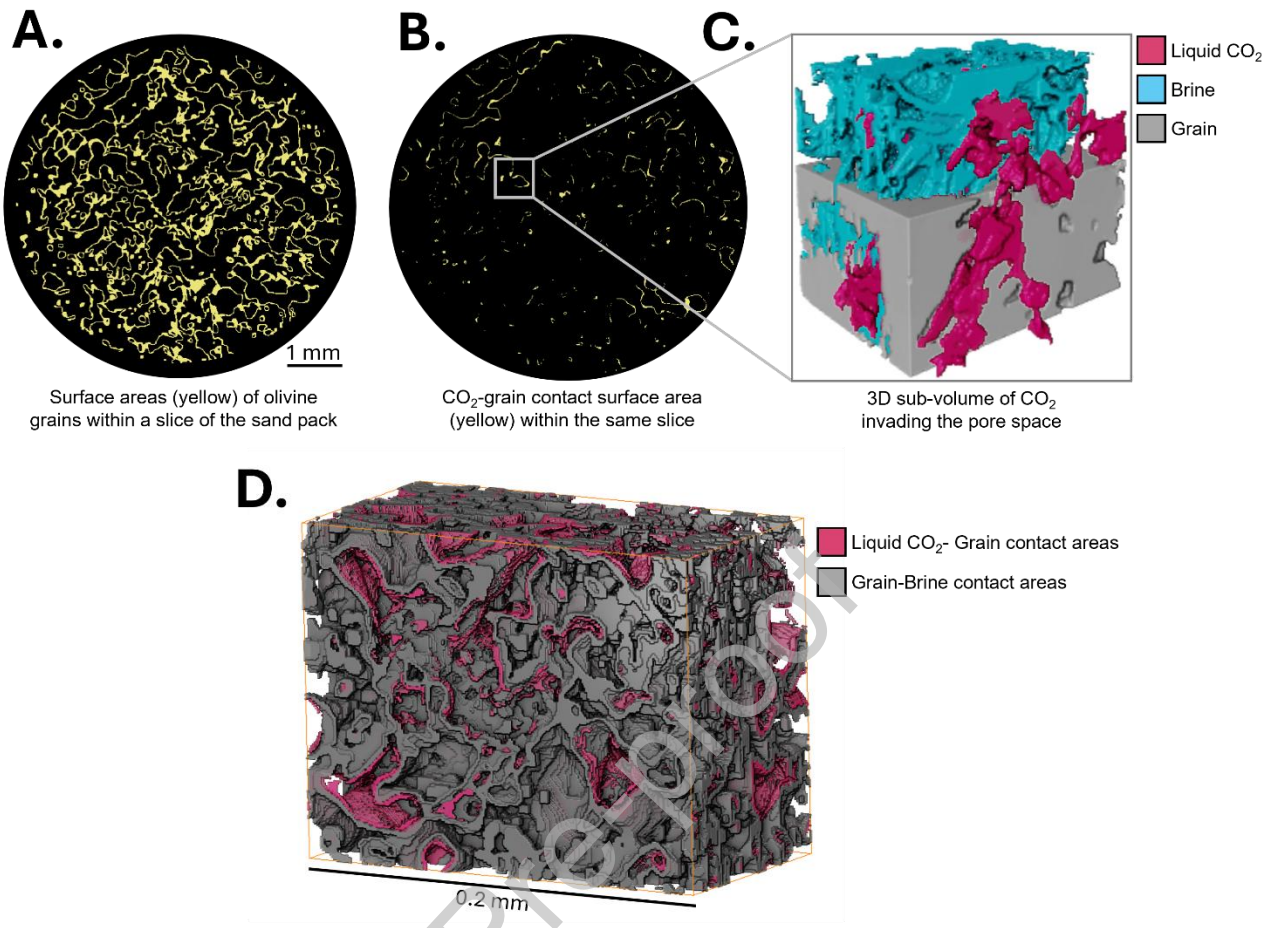

Figure 9. 2D cross section image slices taken from the olivine grain pack during co-injection using a half bar entry pressure. A) Highlighted in yellow are the total olivine grain surface area present within each section and B) the equivalent slice showing the corresponding fraction of that surface area which is in direct contact with liquid CO_2. C) A 3D cubic sub-volume taken from the region invaded by CO_2 (outlined in grey in figure B), visualising a pocket of liquid CO_2 occupying inter-granular pore space in direct contact with both the olivine grains and the carbonated brine solution. D) An example 3D sub-volume extracted from the same region of the grain pack, mapping the distribution of CO_2 and brine contact areas with olivine grains.

Magnesium concentrations for the experiments with elevated CO_2 saturations are shown in figure 10. Box plots show the range in concentration from benchmark carbonated water (bulk aqueous) experiments (full control dataset shown in section 2.3), and the curve shows the prediction from a 1-D reactive transport simulation parameterised by standard aqueous dissolution rate law parameters. The experiments with capillary pressure plates and elevated CO_2 saturations, yield leached Mg^{2+} concentrations that are marginally elevated relative to single-phase experiments using carbonated water (fig. 10). The PHREEQC reactive transport simulation reproduces the overall concentration magnitude, validating the experimental setup (Table 4), although it does not capture dynamics likely associated with the evolution of the grain size distribution (see section 2.6).

The experiments with elevated CO_2 saturations demonstrate that dissolution rates are not slower than in the bulk aqueous environment. The observed rates are 1.1-1.2 times, and an average of 1.14 times the carbonated water experiment rates (Table 4). This value represents

the enhancement factor (z), shown in equations 5-7 in section 2.6. When normalised to the fraction of the mineral surface area contacted by the CO_2 phase, the inferred upper-bound dissolution rate is 3.76 (±0.14) times that measured in the bulk aqueous system, with the reported uncertainty incorporating the error propagated from the image segmentation analysis. There is a larger uncertainty, however, because the estimate of the CO_2-mineral contact area was derived from a single image. While the average saturation of fluids in the samples during steady state flow should be constant, it is known that dynamics in the fluid distribution at the pore-network scale may occur and there may have been corresponding fluctuations in the CO_2-mineral contact area. Given this uncertainty, and the increased uncertainty in the elevated saturation observations relative to the single-phase controls, the reaction rates may remain closer to the aqueous benchmark.

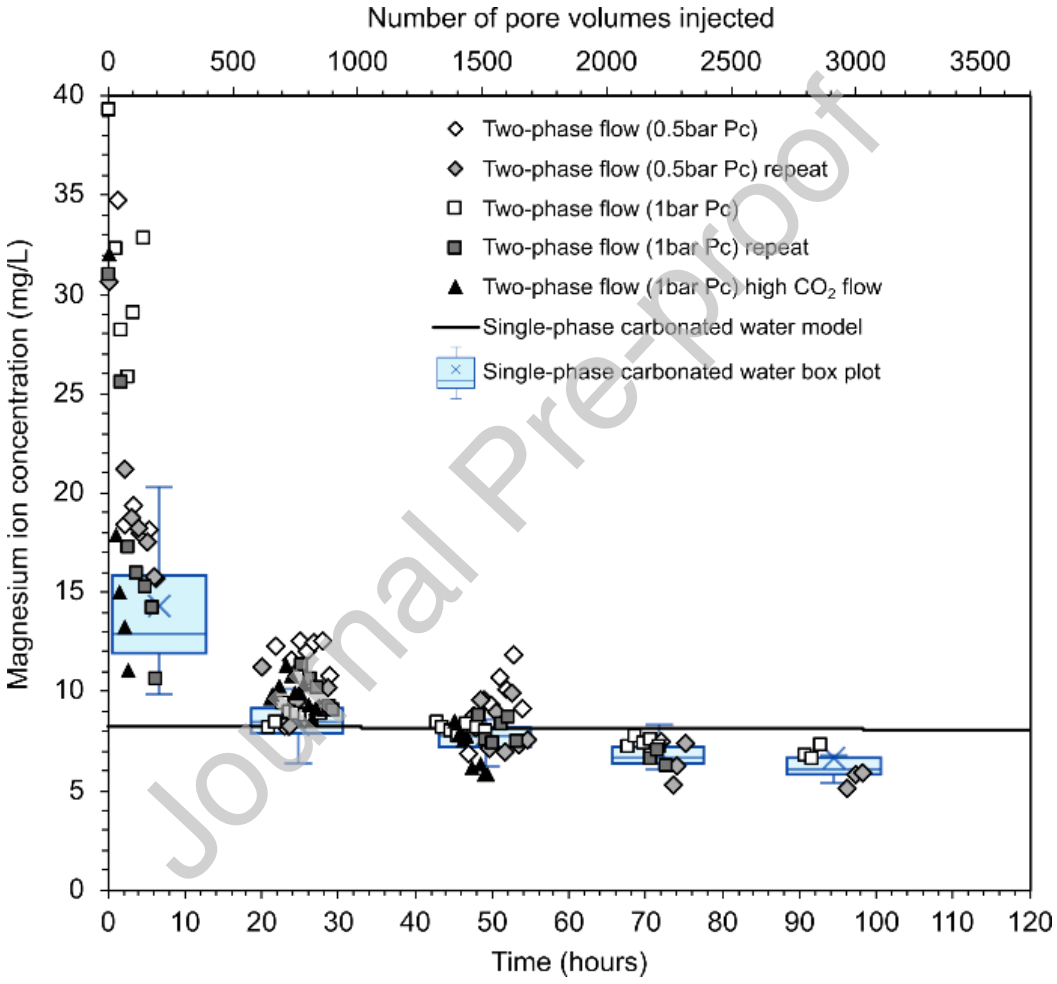

Figure 10. Magnesium concentrations obtained from co-injection (two-phase) experiments, plotted against time and number of pore volumes injected with carbonated water. These experiments were conducted with ceramic porous plates of differing entry pressures as listed. PHREEQC reactive transport model of the bulk aqueous (carbonated water) control dataset is shown as a solid black line. Boxplots from bulk aqueous (single-phase carbonated water injection) experiments are shown in blue for comparison against aqueous dissolution data.

Table 4 – Modelled rates and enhancement factors of two-phase experiments relative to bulk aqueous.

Experiment	Olivine dissolution rate (mol m^{-2} sec^{-1})	Modelled system pH	Rate enhancement factor	Normalised root mean square error

Carbonated water (bulk aqueous)	4.4×10^{-9} – 4.35×10^{-9}	3.275-3.272	-	-
Two-phase co-injection 0.5 bar Pc	5.3×10^{-9} – 5×10^{-9}	3.290-3.286	1.19	0.23
Two-phase co-injection 1 bar Pc	4.9×10^{-9} – 4.7×10^{-9}	3.276-3.273	1.09	0.13
Two-phase co-injection 1 bar Pc & high flow CO_2	5.1×10^{-9} – 4.9×10^{-9}	3.284-3.280	1.15	0.19

Note: To derive rate enhancements in two-phase co-injection experiments; the initial bulk aqueous model rate expression was multiplied by an enhancement factor which minimised least squares error.

3.2 Effect of interfacial water film mobility on reaction rates in wet CO_2 environments

A set of experiments was conducted to evaluate the impact of transport limitations in the water films on reaction rates. In these experiments (ALT1 and ALT2), fluid injection alternated between water-saturated liquid CO_2, either for 4 or 20 hours, flushed with carbonated water over a duration of minutes. During these experiments, liquid CO_2 was injected for 95% of the experiment duration and constitutes the primary fluid flowing through the olivine pack.

The data from these experiments show that the Mg^{2+} increases to high concentration during the period of CO_2 injection after which it is flushed out by a water injection period (supplementary fig. A6). This is expected given the long residence times of the water films formed in the olivine pack. There are two populations of concentration data depending on whether samples were collected after 20 hours or 4 hours of CO_2 injection.

Rates for the alternating injection experiments were derived by normalising the concentration time-series data by the measured (BET) sample surface area and the liquid CO_2 residence time (see section 2.7). To provide a valid comparison of these rates against the aqueous benchmark, dissolution rates for the carbonated water (control) experiments were re-calculated using the same analytical approach outlined in section 2.7. This rate calculation is different to the micro-focus X-ray CT and PHREEQC model-based methodology applied to the continuous co-injection experiments. Resultant rates in the alternating injection experiment are revealed to be much lower than that of the carbonated water controls (fig. 11). The average rate across both liquid CO_2 flow experiments was 5.95 ($\pm$ 0.28) x 10^{-9} mol m^{-2} sec^{-1} (2.5x lower) compared to carbonated water experiments at 1.5 ($\pm$ 0.04) x 10^{-8} mol m^{-2} sec^{-1}. This shows the large impact of inhibiting reaction product transport, and that sustained reaction in thin water films are contingent on those films being mobile.

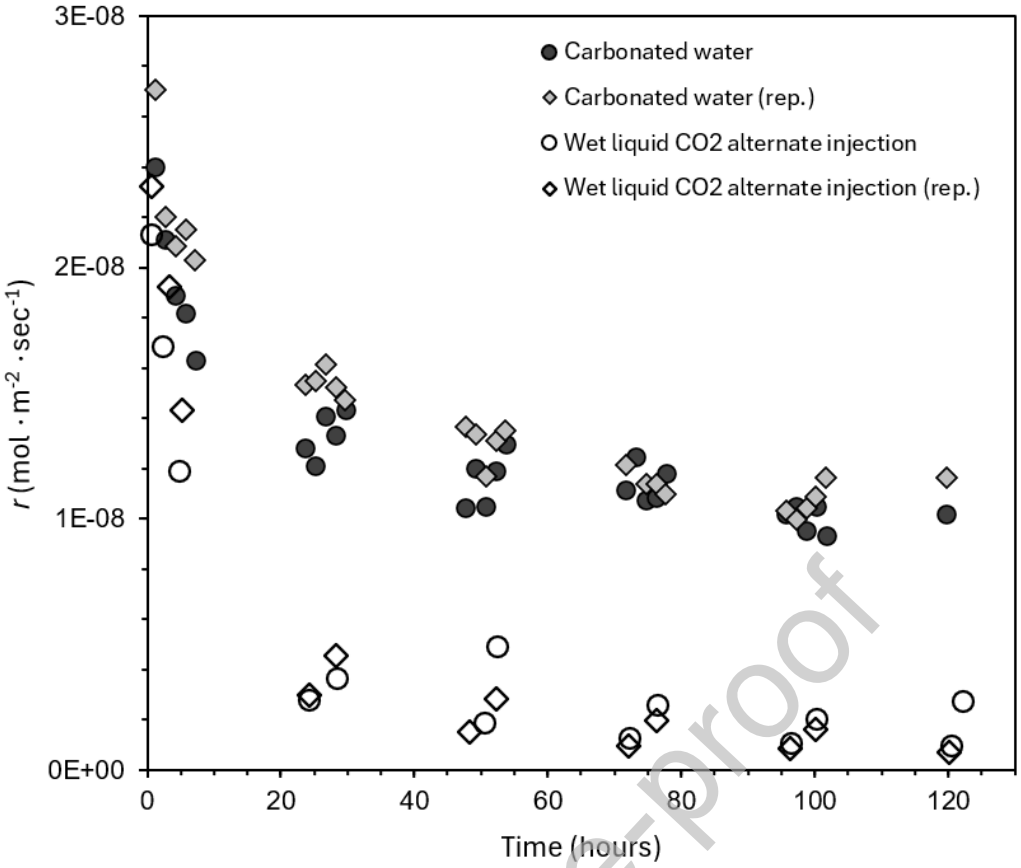

Figure 11. Magnesium release rates normalized by respective fluid residence times and effective surface area, allowing for a direct rate comparison between carbonated water and alternate-flow liquid CO_2 reaction systems.

4. Discussion

4.1 Reaction rates in wet liquid CO_2 match rates in bulk aqueous environments

The co-injection experiments demonstrate that olivine dissolution rates can be sustained under conditions characteristic of direct free-phase CO_2 injection, despite the substantially lower fraction of water present relative to fully (bulk) aqueous systems. A comparison between the bulk aqueous and co-injection experiments is enabled by the consistent conditions maintained across the experiments. Water flow rates and aqueous residence times were held constant between co-injection and single-phase (carbonated water) injection experiments, thereby maintaining an equivalent aqueous mass balance across experiments. Consequently, differences in the measured dissolution rates cannot be attributed to changes in the bulk aqueous transport imposed by the experimental design, but instead reflect differences in the interfacial distribution and mobility of the aqueous phase within the grain pack imposed by the introduction of CO_2. Moreover, the aqueous benchmark employed in the present study is not derived from the literature but from internally consistent aqueous control experiments performed using the same reactor, mineral material, temperature, pressure, residence time, analytical methods and rate normalisation procedures as the CO_2-rich experiments. The comparison therefore isolates the influence of the fluid system while eliminating uncertainties associated with cross-study comparisons. Hence, the observed

dissolution rates provide a direct comparison between bulk aqueous (carbonated water) and CO_2-rich (wet liquid CO_2) environments under otherwise equivalent reaction conditions.

A further consideration is the reactive surface area used to normalise dissolution rates in the co-injection experiments. The *operando* micro-focus X-ray CT imaging approach provides a direct measurement of fluid distributions within the grain pack during steady state pressure conditions (fig. 8). The present analysis is based on the fractional partitioning of the mineral surface between the fluid phases rather than a quantitation of the surface area itself, reducing the sensitivity of the calculated enhancement factors to any residual segmentation uncertainty. The main requirement in this approach is that CT-based surface-area is proportional to the surface area measurement by BET, and this has long been established including in comparisons of surface area measurements of rock materials against BET measurements in Lai et al., (2017) and previously in Kerbrat et al., (2008). Moreover, mass balance (derived from data shown in supplementary figure A5) indicates that only ~2-3% of the initial mineral mass dissolved over the five-day experiments, supporting the assumption that the fluid distributions captured by the operando micro-focus CT imaging remained representative throughout the experiments. This allows dissolution rates to be evaluated with respect to the actively wetted mineral surface rather than the total mineral surface area (fig. 9). When normalised to the fraction of mineral surface area contacted by CO_2, dissolution rates are up to 3.76 times greater than those measured in the bulk aqueous benchmark experiments. This value represents the upper end of the experimentally constrained enhancement range rather than a universal enhancement factor, and may reflect the combined influence of interfacial chemistry, water-film mobility, and solute transport. The normalisation presented here assumes that the additional dissolution is confined to the mineral surface contacted by the CO_2 phase, thereby providing an upper-bound on the local enhancement factor. However, the range of possible enhancement factors includes values that are statistically indistinguishable from the aqueous controls (fig. 10). In practice, intermittent flow can result in fluctuations in CO_2 occupancy and interfacial water distribution may redistribute reactive conditions across a greater proportion of the mineral surface over time (Reynolds et al., 2017), such that the observed bulk enhancement (1.1-1.2 times) may be more representative of the increase in dissolution rate. Accordingly, the precise magnitude of the enhancement is less significant than the observation that elevated CO_2 saturation does not suppress dissolution relative to fully aqueous conditions e.g., due to decreased mineral surface area in contact with the aqueous solution.

The interpretation of the measured dissolution rates is further supported by the experimental design. The strongly acidic conditions maintained throughout the experiments were intentionally selected to isolate the rate-limiting dissolution step of carbon mineralisation. Carbonated water was continuously supplied at operating conditions throughout the experiments, maintaining disequilibrium with respect to olivine dissolution and limiting the accumulation of dissolved reaction products within the reactor. Under these conditions, dissolution rather than secondary mineral precipitation is expected to control the measured reaction rates. Magnesium was selected as the primary dissolution tracer because it provides the most direct measure of olivine dissolution under these conditions. Using PHREEQC

simulations we estimate that measured Mg^{2+} concentrations remained approximately two orders of magnitude below the equilibrium concentrations required for magnesite precipitation and five orders of magnitude below those for brucite. This provides further support that dissolution, rather than secondary precipitation, controlled the measured aqueous chemistry. Post-reaction XRD patterns from each experimental configuration also show no evidence that additional precipitate formed (supplementary figure A7). This distinction is important because precipitation reactions may otherwise impact the measured Mg^{2+} signal, and precipitation reactions can be influenced by contaminants leached from reactor materials, including Ni-bearing Hastelloy components (fig. 5) (Caulfield et al., 2023). While such effects may be relevant in studies focused on carbonate precipitation, the present experiments were specifically designed to isolate dissolution kinetics under continuous-flow conditions. The measured rates therefore represent a direct assessment of olivine reactivity in wet CO_2 environments. Taken together, these observations demonstrate that rapid olivine dissolution can be maintained despite reduced water content within the olivine grain pack. The significance of this result is not simply that dissolution occurs in wet CO_2, but that dissolution proceeds at rates comparable to, and potentially exceeding, those measured under fully aqueous conditions. The reported enhancement factors should therefore be interpreted relative to the equivalent aqueous experiments conducted under the same temperature, pressure, and water residence time, with the mode of fluid injection, and consequently the distribution of CO_2 and interfacial water, representing the principal experimental variable. The data indicate that reaction within flowing microscale water films contributes to macroscopic dissolution kinetics and show that the presence of a continuous bulk aqueous phase is not a prerequisite for sustained geochemical reaction. Previous studies have sought to maintain rapid mineralisation kinetics through the injection and recirculation of large volumes of carbonated water (Matter et al., 2011; Oelkers et al., 2026). The present results demonstrate that comparable dissolution rates can be achieved in CO_2-rich systems despite lower water content, provided that connected and mobile interfacial water films are maintained. The specific mechanism underpinning a rate enhancement requires further investigation. However, the chemical environment of thin water films on forsterite under these conditions is distinct from bulk aqueous environments in ways that offer a number of potential reaction paths through which dissolution rates may be enhanced (Abdolhosseini et al., 2022). In particular, CO_2-rich interfacial water can exhibit distinct carbonic-acid formation, proton activity and ion solvation behaviour relative to bulk aqueous solutions, while continuous renewal of the films can maintain supply of reactive CO_2-rich water and removal of dissolved reaction products. These findings support reactive transport approaches in which mineral dissolution rates are not prescribed as a direct function of fluid saturation alone. Similarly, pore-scale models that depict water as incapable of forming continuous reactive interfaces (Lan et al., 2025) should be further developed to account for dissolution occurring within connected and flowing water films. The observations therefore suggest that bulk water saturation is insufficient to predict reactivity in CO_2-rich environments and its role in governing reaction kinetics requires further investigation.

4.2 Reaction rates in water films are inhibited when there are transport limitations

The observations presented in figure 11 (and supplementary figure A6) provide insight into the mechanism responsible for sustaining rapid olivine dissolution in wet CO_2 environments. The results demonstrate that the presence of water films alone are insufficient to maintain reaction kinetics. Instead, sustained dissolution requires the continued transport of dissolved reaction products away from the mineral surface via interfacial water films that are mobile. When water mobility is restricted, reaction rates decrease despite the continued presence of water-bearing liquid CO_2, indicating that reactant transport within the aqueous phase exerts a primary control on reactivity under these conditions.

Results from alternating fluid injection experiments, where water films are only replenished episodically (fig. 7), provide direct evidence for this behaviour. In these experiments, dissolution rates were substantially lower than those observed in both the aqueous benchmark and co-injection experiments. The limited volume of stagnant interfacial water results in local accumulation of dissolved reaction products (i.e., magnesium) at the mineral surface. The recovered samples did not directly capture these *in situ* concentrations, rather they were obtained by flushing the reactor with water and were consequently diluted relative to the reacting films. The *in situ* Mg^{2+} concentrations within the stagnant films were therefore likely higher than those measured in the recovered samples. The accumulation of dissolved reaction products and associated increase in pH provide a mechanistic explanation for the suppressed dissolution rates observed under alternating injection conditions. This interpretation is further supported by reactive transport modelling. Reducing the water flow rate by an order of magnitude in the PHREEQC model increased the residence time sufficiently to reproduce the upper-bound Mg^{2+} concentrations measured in the alternating injection experiments (ALT1,2), corresponding to a pH of 3.8 and a 1.8-2.3x reduction in the predicted dissolution rate. The prolonged residence time model shows effluent fluids remain strongly undersaturated with respect to forsterite, with the saturation index increasing from −29.42 to −26.58 under continuous-flow conditions to −25.70 to −22.03 under prolonged water residence time conditions. The effect of longer residence time on the dissolution rate is thus primarily due to the pH increase with reaction progress, and the corresponding reduction in rate. In contrast, dynamically renewed films may continuously remove reaction products and supply CO_2-rich acidic water, maintaining dissolution rates comparable to, or potentially greater than, those measured in fully aqueous systems.

The alternating injection experiments were designed to isolate the impacts of the interfacial water film mobility. The co-injection and alternating injection experiments were performed under the same temperature, pressure, reactor configuration, sample mass, mineralogy and water flow rate, with the pattern of fluid injection representing the principal experimental variable. Consequently, the distinguishing feature between the experiments is the mobility of water and the interfacial water films. This interpretation is reinforced by the reproducible temporal response observed during the alternating injection experiments (see supplementary figure A6). The repeated aqueous Mg^{2+} concentration pattern (high Mg after ~20 h CO_2 exposure, low Mg after 4 h CO_2 exposure) shows that the system responds reversibly to the injection schedule. If intrinsic limitations such as substantial changes in reactive surface area, or olivine dissolution naturally approaching equilibrium across the grain-pack were the

dominant control, a progressive temporal trend would be expected as the experiment proceeded. Instead, we record two reproducible groups of magnesium concentration data clearly linked to the two lengths of exposure period used. Collectively, these observations indicate that transport of dissolved reaction products within stagnant interfacial water films provides the most consistent explanation for the observed reduction in dissolution rates. This observation provides an important context for interpreting previous studies of water-bearing CO_2 reactivity. Investigations of thin water films formed in water-bearing CO_2 have almost exclusively employed static batch-reactor configurations (Felmy et al., 2012; Loring et al., 2012; Schaef et al., 2013; Rajan et al., 2025). In such systems, solute transport away from reaction sites is limited, making it difficult to distinguish between effects arising from fluid composition and those arising from transport constraints. In contrast, the co-injection experiments designed and presented here maintain connected and flowing water films, allowing dissolution rates to be quantified under conditions where transport limitations are minimised. The suppressed reactivity of minerals in wet CO_2 relative to bulk aqueous environments reported in some previous studies may therefore reflect local saturation of interfacial water films rather than an intrinsic limitation on geochemical reactions taking place in water-bearing liquid or supercritical CO_2 environments.

In contrast, water films in capillary-dominated porous media are not necessarily static. Wetting films within subsurface rocks commonly form connected flow pathways and constitute an important component of water transport in hydrogeological systems (Blunt, 2017). The distinction between isolated and mobile interfacial films is therefore critical. While both may initially support mineral dissolution, only mobile films can sustain reaction over extended timescales by continually replenishing reactive fluid and transporting dissolved products away from the mineral surface. Consequently, the porous plates employed in the co-injection experiments were used to establish a capillary-controlled fluid configuration in which connected interfacial water films could be sustained and investigated under well-defined conditions. Although reservoir-scale fluid distributions are additionally influenced by buoyancy, gravity and geological heterogeneity, field observations from geological CO_2 storage reservoirs demonstrate that sustained free-phase CO_2 saturations can develop within the subsurface (Cowton et al., 2016). Connected wetting films therefore remain a fundamental feature of capillary-dominated porous media wherever a wetting aqueous phase coexists with free-phase CO_2. The present experiments therefore isolate the influence of this interfacial environment on olivine dissolution rather than attempting to reproduce the full complexity of reservoir-scale multiphase flow.

This interpretation reconciles the contrasting observations obtained in the co-injection and alternating injection experiments. In the co-injection experiments, connected and flowing interfacial water films maintained transport between reaction sites and the bulk fluid, enabling measurement of true dissolution rates in thin films, which are comparable to or exceeding those measured under fully aqueous conditions. In the alternating injection experiments, transport limitations developed within the interfacial water phase, resulting in slower dissolution kinetics despite the continued presence of water. Collectively, the results presented here suggest that the mobility of interfacial water films, rather than the total

quantity of water present, is the primary control on dissolution kinetics in wet CO_2 environments. Whilst the findings of this study are established under controlled experimental conditions, the broader implication is that subsurface flow regimes capable of sustaining mobile, well-connected wetting films may maximise mineral dissolution while substantially reducing water requirements for engineered CO_2 mineralisation.

5. Conclusion

The experimental results show that the rate-limiting dissolution step governing carbon mineralisation in basalts is not slower when CO_2 is injected directly into the subsurface than when it is first dissolved in water. Co-injection of water and liquid CO_2 at elevated capillary pressure resulted in olivine dissolution rates matching or exceeding aqueous rates by up to 3.76 times. These findings resolve a major uncertainty surrounding geological carbon mineralisation in CO_2-rich environments and demonstrate that direct CO_2 injection can sustain the rate-limiting mineral dissolution process while substantially reducing water demand. Because aqueous mineralisation approaches require large volumes of water for CO_2 dissolution prior to injection, direct injection may alleviate important practical constraints on freshwater consumption, fluid handling, and reservoir injectivity during large-scale deployment of geological carbon removal.

The study further shows that reactivity in wet CO_2 environments is governed by the mobility and connectivity of interfacial water films rather than total water content alone. We demonstrate that reactivity is inhibited when interfacial water films are static, with dissolution rates falling below those measured in both flowing water-film (co-injection) experiments, and fully aqueous systems. Experimental characterisation of these reaction environments must therefore distinguish between observations with and without transport limitations. When interfacial water films remain connected and flowing, as expected in permeable subsurface reservoirs, rapid reaction kinetics persist. These findings have important implications for the design and operation of engineered carbon mineralisation systems and indicate that direct free-phase CO_2 injection into reactive basalt formations may provide a scalable route for permanent carbon storage with lower water requirements and without sacrificing mineralisation rates.

Acknowledgments

The author acknowledges financial support from the Shell InFUSE Prosperity Partnership and the Engineering and Physical Sciences Research Council (EPSRC, grant no. EP/V038044/1). The authors also thank Sibelco Nordic AS for providing the samples used in this study, as well as Dr. Sojwal Manoorkar and Dr. Atefeh Vafaie.

Author Contributions

Mohamed A. Saleh: Conceptualization, Investigation, Methodology, Software, Validation, Formal analysis, Visualization, Data curation and Writing-original draft. **J.P. Martin Trusler**: Methodology, Supervision, and Writing-review and editing. **Mary P. Ryan**: Supervision. **Nihal Darraj**: Investigation and Software. **Samuel Krevor**: Conceptualization, Investigation, Methodology, Resources, Supervision, Funding acquisition, and Writing-review and editing.

Competing interests

The authors declare no competing financial interest.

Data availability

All data are available in the Article and its Supplementary Information. Source data are provided with this paper.

Appendix A. Supplementary Material

Figures and data tables containing additional experimental details, materials, and methods relating to this study are provided in the supplementary information sheet.

References

1. Aavatsmark, I. & Kaufmann, R. (2015) A simple function for the solubility of water in dense-phase carbon dioxide. *International Journal of Greenhouse Gas Control.* 32 47–55.
2. Abdolhosseini Qomi M. J.; Miller Q.R.; Zare S.; Schaef H.T.; Kaszuba J.P.; Rosso K. M. (2022) Molecular-scale mechanisms of CO_2 mineralisation in nanoscale interfacial water films. NatRevChem; 6(9): 598–613.
3. Blunt, M. J. (2017) *Multiphase flow in permeable media: A pore-scale perspective. [Google Scholar]* Cambridge university press.
4. Caulfield, B., Roberts, M. & Prigiobbe, V. (2023) Studying the effect of nickel, copper, and zinc on the precipitation kinetics and the composition of Ca-carbonates for the integrated process of CO_2 mineralization and brine mining. *Chemical Engineering Journal.* 476 146220. 10.1016/j.cej.2023.146220.
5. Chen, Q. & Trusler, J. P. M. (2025) Olivine dissolution kinetics at elevated temperatures and pressures. *Chemical Engineering Journal.* 525 169095. 10.1016/j.cej.2025.169095.
6. Cowton, L. R., Neufeld, J. A., White, N. J., Bickle, M. J., White, J. C. & Chadwick, R. A. (2016) An inverse method for estimating thickness and volume with time of a thin CO2-filled layer at the Sleipner Field, North Sea. *Journal of Geophysical Research: Solid Earth.* 121 (7), 5068–5085.
7. Felmy, A.R., Qafoku, O., Arey, B.W., Hu, J.Z., Hu, M., Todd Schaef, H., Ilton, E.S., Hess, N.J., Pearce, C.I., Feng, J. & Rosso, K.M. (2012) Reaction of water-saturated supercritical CO_2 with forsterite: Evidence for magnesite formation at low temperatures. *Geochimica et Cosmochimica Acta*. 91, 271–282. doi:10.1016/j.gca.2012.05.026.
8. Gadikota, G., Matter, J., Kelemen, P. & Park, A. (2014) Chemical and morphological changes during olivine carbonation for CO_2 storage in the presence of NaCl and NaHCO sub(3). Physical Chemistry Chemical Physics: PCCP. 16 (10), 4679-4693. 10.1039/c3cp54903h.
9. Garfi, G., John, C. M., Berg, S. & Krevor, S. (2020) The sensitivity of estimates of multiphase fluid and solid properties of porous rocks to image processing. *Transport in Porous Media.* 131 (3), 985–1005.
10. Garfi, G., John, C. M., Lin, Q., Berg, S. & Krevor, S. (2020) Fluid surface coverage showing the controls of rock mineralogy on the wetting state. *Geophysical Research Letters.* 47 (8), e2019GL086380.
11. [b] Garfi, G., John, C. M., Rücker, M., Lin, Q., Spurin, C., Berg, S. & Krevor, S. (2022) Determination of the spatial distribution of wetting in the pore networks of rocks. *Journal of Colloid and Interface Science.* 613 786–795. 10.1016/j.jcis.2021.12.183.
12. Gerdemann, S. J., O'Connor, W. K., Dahlin, D. C., Penner, L. R. & Rush, H. (2007) Ex situ aqueous mineral carbonation. *Environmental Science & Technology.* 41 (7), 2587–2593.

13. Hänchen, M., Prigiobbe, V., Storti, G., Seward, T. M. & Mazzotti, M. (2006) Dissolution kinetics of fosteritic olivine at 90–150°C including effects of the presence of CO_2. *Geochimica Et Cosmochimica Acta.* 70 (17), 4403–4416. 10.1016/j.gca.2006.06.1560.
14. Harned, H. S., & Owen, B. B. (1958). The Physical Chemistry of Electrolytic Solutions. New York: Reinhold Publishing.
15. Hua, Y, Barker, R, Neville, A. (2015) Comparison of corrosion behaviour for X-65 carbon steel in supercritical CO_2-saturated water and water-saturated/unsaturated supercritical CO_2. J Supercrit Fluids 97, 224–37.
16. Johnson, N. C., Thomas, B., Maher, K., Rosenbauer, R. J., Bird, D. & Brown, G. E. (2014) Olivine dissolution and carbonation under conditions relevant for *in situ* carbon storage. Chemical Geology. 373 93-105. 10.1016/j.chemgeo.2014.02.026.
17. Keefner, J. W., Mackwell, S. J., Kohlstedt, D. L. & Heidelbach, F. (2011) Dependence of dislocation creep of dunite on oxygen fugacity: Implications for viscosity variations in Earth's mantle. *Journal of Geophysical Research: Solid Earth.* 116 (B5).
18. Kerbrat, M., Pinzer, B., Huthwelker, T., Gäggeler, H. W., Ammann, M. & Schneebeli, M. (2008) Measuring the specific surface area of snow with X-ray tomography and gas adsorption: comparison and implications for surface smoothness. *Atmospheric Chemistry and Physics.* 8 (5), 1261–1275..
19. King, M. B., Mubarak, A., Kim, J. D. & Bott, T. R. (1992) The mutual solubilities of water with supercritical and liquid carbon dioxides. *The Journal of Supercritical Fluids.* 5 (4), 296–302. 10.1016/0896-8446(92)90021-B.
20. Lai, P., Moulton, K. & Krevor, S. (2015) Pore-scale heterogeneity in the mineral distribution and reactive surface area of porous rocks. *Chemical Geology.* 411 260–273.
21. Lan, T., Hu, R. & Zhao, B. (2025) Impact of pore-scale corner and film flows on macroscopic transport in porous media. *Capillarity.* 16 (1), 1–4.
22. Li, X., Shen, X., Wang, Q., Lu, D., Qian, B., Pedrosa, E. T. & Luttge, A. (2024) Influence of surface orientation on the variability of olivine dissolution rates. Applied Surface Science. 655 159634. 10.1016/j.apsusc.2024.159634.
23. Loring, J. S., Miller, Q. R., Thompson, C. J. & Schaef, H. T. (2019) Experimental studies of reactivity and transformations of rocks and minerals in water-bearing supercritical CO_2. In: Anonymous Science of carbon storage in deep saline formations. , Elsevier. pp. 63–88.
24. Loring, J. S., Thompson, C. J., Zhang, C., Wang, Z., Schaef, H. T. & Rosso, K. M. (2012) *In situ* infrared spectroscopic study of brucite carbonation in dry to water-saturated supercritical carbon dioxide. The Journal of Physical Chemistry A. 116 (19), 4768-4777.
25. Luhmann, A. J., Tutolo, B. M., Bagley, B. C., Mildner, D. F. R., Seyfried, W. E. & Saar, M. O. (2017) Permeability, porosity, and mineral surface area changes in basalt cores induced by reactive transport of CO_2 -rich brine. American Geophysical Union (AGU).
26. Mahzari, P., Kolahchian, E., Al Mani, S., Fonseca, R. M., Al Jaberi, A., Oasim, A. M., Abdeen, N. S. & Matter, J. M. (2025) Characterizing flow paths in peridotite formations for CO2 sequestration: hydro-mechanical modelling of a pilot test in the UAE. *SPE/AAPG/SEG Carbon, Capture, Utilization, and Storage Conference and Exhibition.* , SPE. pp.D031S029R001.
27. Martinez, R. E., Weber, S. & Bucher, K. (2014) Quantifying the kinetics of olivine dissolution in partially closed and closed batch reactor systems. Chemical Geology. 367 1-12.
28. Matter, J. M., Broecker, W. S., Gislason, S. R., Gunnlaugsson, E., Oelkers, E. H., Stute, M., Sigurdardóttir, H., Stefansson, A., Alfreðsson, H. A. & Aradóttir, E. S. (2011) The CarbFix Pilot Project–storing carbon dioxide in basalt. *Energy Procedia.* 4 5579–5585.
29. Matter, J. M., Stute, M., Snæbjörnsdottir, S. Ó, Oelkers, E. H., Gislason, S. R., Aradottir, E. S., Sigfusson, B., Gunnarsson, I., Sigurdardottir, H. & Gunnlaugsson, E. (2016) Rapid carbon mineralization for permanent disposal of anthropogenic carbon dioxide emissions. *Science.* 352 (6291), 1312–1314.
30. Menefee, A. H. & Schwartz, B. A. (2024) Quantifying the Value of Geologic Carbon Mineralization for Project Risk Management in Carbon Capture and Removal Pathways. Energy & Fuels. 38 (6), 5365–5373.

31. Menefee, A. H., Giammar, D. E. & Ellis, B. R. (2018) *Permanent CO_2 Trapping through Localized and Chemical Gradient-Driven Basalt Carbonation.* American Chemical Society (ACS).
32. Metz, V. & Ganor, J. (2001) Stirring effect on kaolinite dissolution rate. *Geochimica Et Cosmochimica Acta.* 65 (20), 3475–3490. 10.1016/S0016-7037(01)00686-X.
33. Moita, P., Berrezueta, E., Abdoulghafour, H., Beltrame, M., Pedro, J., Mirão, J., Miguel, C., Galacho, C., Sitzia, F., Barrulas, P. & Carneiro, J. (2020) Mineral Carbonation of CO_2 in Mafic Plutonic Rocks, II—Laboratory Experiments on Early-Phase Supercritical CO_2–Brine–Rock Interactions. Applied Sciences. 10 (15), 5083. doi:10.3390/app10155083.
34. Norton, H., Gillessen, P. & Crawford, C. (2024) Techno-economic assessment of supercritical, cold liquid, and dissolved CO_2 injection into sub-seafloor basalt. *Carbon Capture Science & Technology.* 13 100236. 10.1016/j.ccst.2024.100236.
35. Oelkers, E. H., Arkadakskiy, S., Ahmed, Z., Kunnummal, N., Fedorik, J., Marchesi, M., Addassi, M., Omar, A., Menegoni, N. & Gislason, S. R. (2026) CO_2 subsurface mineral storage by its co-injection with recirculating water. *Nature.* 651 (8107), 954–958.
36. Palandri, J. L. & Kharaka, Y. K. (2004) No title. *A Compilation of Rate Parameters of Water-Mineral Interaction Kinetics for Application to Geochemical Modeling.* .
37. Parkhurst, D. L. & Appelo, C. (2013) Description of input and examples for PHREEQC version 3—a computer program for speciation, batch-reaction, one-dimensional transport, and inverse geochemical calculations. *US Geological Survey Techniques and Methods.* 6 (A43), 497.
38. Rajan, B. P., Mergelsberg, S. T., Bowden, M. E., Peterson, K. A., Burton, S. D., Bowers, G. M., Wietsma, T. W., Graham, T. R., Qafoku, O. & Thompson, C. J. (2025) Decreasing Hygroscopicity Slows Forsterite Carbonation under Low-Water Conditions. *Environmental Science & Technology.*
39. Rangel-Jurado, N., Kong, X., Kottsova, A., Grafulha Morales, L., Ma, N., Games, F., Brehme, M., Bernasconi, S. M. & Saar, M. O. (2025) Reactivity of wet $ScCO_2$ toward reservoir and caprock formations under elevated pressure and temperature conditions: Implications for CCS and CO_2-based geothermal energy extraction. *Energy & Fuels.* 39 (3), 1679–1693.
40. Ratouis, T. M., Snæbjörnsdóttir, S. Ó, Voigt, M. J., Sigfússon, B., Gunnarsson, G., Aradóttir, E. S. & Hjörleifsdóttir, V. (2022) Carbfix 2: A transport model of long-term CO_2 and H2S injection into basaltic rocks at Hellisheidi, SW-Iceland. International Journal of Greenhouse Gas Control. 114 103586.
41. Reynolds, C. A., Menke, H., Andrew, M., Blunt, M. J. & Krevor, S. (2017) Dynamic fluid connectivity during steady-state multiphase flow in a sandstone. *Proceedings of the National Academy of Sciences.* 114 (31), 8187–8192.
42. Saleh, M. A., Ryan, M. P., Trusler, J. P. M. & Krevor, S. (2025) The interfacial processes controlling carbon dioxide mineralisation in magnesium and calcium silicates. Fuel. 380 132969. 10.1016/j.fuel.2024.132969.
43. Saleh, M. A., Shiel, H., Ryan, M. P., Trusler, J. M. & Krevor, S. (2024) Enhanced olivine reactivity in wet supercritical CO_2 for engineered mineral carbon sequestration. *Energy & Fuels.* 38 (21), 21028–21041.
44. Schaef, H. T., McGrail, B. P., Loring, J. L., Bowden, M. E., Arey, B. W. & Rosso, K. M. (2013) Forsterite [Mg_2SiO_4)] Carbonation in Wet Supercritical CO_2: An *in Situ* High-Pressure X-ray Diffraction Study. *Environmental Science & Technology.* 47 (1), 174-181. 10.1021/es301126f.
45. Snæbjörnsdóttir, S. Ó, Sigfússon, B., Marieni, C., Goldberg, D., Gislason, S. R. & Oelkers, E. H. (2020) Carbon dioxide storage through mineral carbonation. https://discovery.ucl.ac.uk/id/eprint/10096305.
46. van Noort, R., Spiers, C. J., Drury, M. R. & Kandianis, M. T. (2013) Peridotite dissolution and carbonation rates at fracture surfaces under conditions relevant for *in situ* mineralization of CO_2. *Geochimica Et Cosmochimica Acta.* 106 1–24. 10.1016/j.gca.2012.12.001.
47. Wang, F., Dreisinger, D., Jarvis, M. & Hitchins, T. (2019) Kinetics and mechanism of mineral carbonation of olivine for CO_2 sequestration. Minerals Engineering. 131 185-197.
48. [b] Wang, F., Dreisinger, D., Jarvis, M., Hitchins, T. & Dyson, D. (2019) Quantifying kinetics of mineralization of carbon dioxide by olivine under moderate conditions. *Chemical Engineering Journal.* 360 452–463.

49. Wolff-Boenisch, D. & Galeczka, I. M. (2018) Flow-through reactor experiments on basalt-(sea) water-CO_2 reactions at 90° C and neutral pH. What happens to the basalt pore space under post-injection conditions? International Journal of Greenhouse Gas Control. 68 176–190.

Graphical abstract

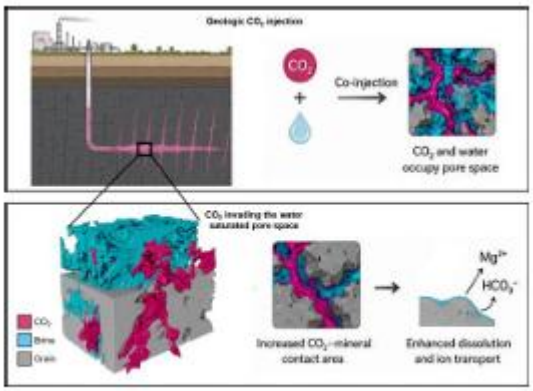

Declaration of interests

☒ The authors declare that they have no known competing financial interests or personal relationships that could have appeared to influence the work reported in this paper.

☐ The authors declare the following financial interests/personal relationships which may be considered as potential competing interests: